

Conn: A Functional Connectivity Toolbox for Correlated and Anticorrelated Brain Networks

Susan Whitfield-Gabrieli and Alfonso Nieto-Castanon

Abstract

Resting state functional connectivity reveals intrinsic, spontaneous networks that elucidate the functional architecture of the human brain. However, valid statistical analysis used to identify such networks must address sources of noise in order to avoid possible confounds such as spurious correlations based on non-neuronal sources. We have developed a functional connectivity toolbox *Conn* (www.nitrc.org/projects/conn) that implements the component-based noise correction method (CompCor) strategy for physiological and other noise source reduction, additional removal of movement, and temporal covariates, temporal filtering and windowing of the residual blood oxygen level-dependent (BOLD) contrast signal, first-level estimation of multiple standard functional connectivity magnetic resonance imaging (fcMRI) measures, and second-level random-effect analysis for resting state as well as task-related data. Compared to methods that rely on global signal regression, the CompCor noise reduction method allows for interpretation of anticorrelations as there is no regression of the global signal. The toolbox implements fcMRI measures, such as estimation of seed-to-voxel and region of interest (ROI)-to-ROI functional correlations, as well as semipartial correlation and bivariate/multivariate regression analysis for multiple ROI sources, graph theoretical analysis, and novel voxel-to-voxel analysis of functional connectivity. We describe the methods implemented in the *Conn* toolbox for the analysis of fcMRI data, together with examples of use and interscan reliability estimates of all the implemented fcMRI measures. The results indicate that the CompCor method increases the sensitivity and selectivity of fcMRI analysis, and show a high degree of interscan reliability for many fcMRI measures.

Key words: brain connectivity; CompCor functional connectivity; intrinsic connectivity; noise; resting state

Introduction

FUNCTIONAL CONNECTIVITY HAS BEEN broadly defined to be the statistical association (or temporal correlation) among two or more anatomically distinct regions (or remote neurophysiological events) (Friston et al., 1994; Horwitz, 2003; Salvador et al., 2005). Numerous methods have been used to investigate these temporal correlations, including independent component analysis (ICA) (e.g., Beckmann et al., 2005; Calhoun et al., 2001, 2004), seed-driven functional connectivity magnetic resonance imaging (fcMRI) (e.g., Biswal et al., 1995; Fox et al., 2005; Greicius et al., 2003), and psychophysiological interactions used to characterize activation in a particular brain region in terms of the interaction between the influence of another area and an experimental parameter (Friston et al., 1997; Gitelman et al., 2003). Functional connectivity has been investigated in block (e.g., Hampson et al., 2002; Koshino et al., 2005) and event-related (Aizenstein et al., 2009; Fox et al., 2006; Rissman et al., 2004; Siegle et al.,

2007) fMRI activation designs. Further, functional connectivity is evident during rest in the absence of task-related activation (Biswal et al., 1995).

Low-frequency resting state networks (<0.1 Hz) reveal coherent, spontaneous fluctuations that delineate the functional architecture of the human brain (Biswal et al., 1995, 2010; Buckner et al., 2008; Fox et al., 2005; Fox and Raichle, 2007). Such networks were initially discovered for the motor system (Biswal et al., 1995), but have also been discovered for both task-positive and task-negative (i.e., default, Raichle et al., 2001) neural systems (Fox et al., 2005; Fransson, 2005; Kelly et al., 2008; Uddin et al., 2009). Resting state networks have been shown to be robust and reliable (Chen et al., 2008; Damoiseaux et al., 2006; Shehzad et al., 2009; Zuo et al., 2010a, 2010b), and to exist in infants (Fransson et al., 2007), during sleep (Fukunaga et al., 2006; Horowitz et al., 2008), under light sedation (Greicius et al., 2008) and under anesthesia in primates (Vincent et al., 2007). Such networks have been associated with individual differences in healthy people (Mennes

Department of Brain and Cognitive Sciences, Martinos Imaging Center at McGovern Institute for Brain Research, and Poitras Center for Affective Disorders Research, Massachusetts Institute of Technology, Cambridge, Massachusetts.

et al., 2010). Because rest has no behavioral demands, resting state connectivity is particularly useful for characterizing functional brain network differences in pediatric and clinical populations, such as schizophrenia (Whitfield-Gabrieli et al., 2009; Whitfield-Gabrieli and Ford 2012), ADHD (Castellanos et al., 2008), autism (Weng et al., 2010), depression (Greicius et al., 2007; Hamilton et al., 2011), bipolar disorder (Chai et al., 2012), and Alzheimer's disease (Buckner et al., 2009; Greicius et al., 2004; Wang et al., 2007).

The two most common analytical approaches toward analyzing resting state functional connectivity (RSFC) data are ICA (e.g., Beckmann et al., 2005, 2009; Greicius et al., 2007; Stevens et al., 2009) and seed-driven RSFC (e.g., Biswal et al., 1995; Castellanos et al., 2008; Greicius et al., 2003; Fox et al., 2005). In seed-driven RSFC analysis, Pearson's correlation coefficients are calculated between the seed time course and the time course of all other voxels, after which correlation coefficients are typically converted to normally distributed scores using Fisher's transform to allow for second-level General Linear Model analysis. Correlation maps often depend on the specific location of the seed, so that seed-driven RSFC has been used to dissociate functionally and anatomically heterogeneous regions of interest (Di Martino et al., 2008; Margulies et al., 2007; Roy et al., 2009; Uddin et al., 2010), and to delineate functional topography in the brain by sharp transitions in correlation patterns that signal functional boundaries across cortex (Cohen et al., 2008).

In functional connectivity analysis, it is critical to appropriately address noise in order to avoid possible confounding effects (spurious correlations based on non-neuronal sources). Standard methods dealing with blood oxygen level-dependent (BOLD) contrast signal noise sources that may be appropriate in the context of the estimation of task- or condition-dependent BOLD signal responses (e.g., regression of subject movement parameters in standard functional analysis) may not suffice in the context of the estimation of functional connectivity measures. For activation studies, the risk of only partially removing BOLD signal noise sources is typically a potential decrease of sensitivity (increasing type II errors), whereas for resting connectivity studies, the risk is a potential decrease of validity (increasing type I errors). Therefore, a more conservative approach to controlling the effects of BOLD signal noise sources is warranted in the context of functional connectivity analysis compared with that of standard functional analysis. In Chai et al. (2012) we showed how a method for reducing spurious sources of variance in BOLD and perfusion-based fMRI, the anatomical component-based noise correction method (aCompCor) (Behzadi et al., 2007), can be particularly useful in the context of fcMRI analysis, increasing not only the validity, but also the sensitivity and specificity of these analyses. Compared to methods that subtract global signals from noise regions of interest (ROIs), the CompCor method is more flexible in its characterization of noise. It models the influence of noise as a voxel-specific linear combination of multiple empirically estimated noise sources, which are estimated from the variability in BOLD responses within noise ROIs. This is particularly appropriate for fMRI noise sources as cardiac and respiratory effects do not have a common spatial distribution in their effects (e.g., cardiac effects are particularly visible near vessels and respiratory effects appear more globally and stronger near edges in the image). Removal of this richer characteriza-

tion of the range of voxel-specific noise effects and additional movement and possible task-related covariates, together with temporal filtering and windowing of the resulting BOLD signal at each voxel, provides increased protection against possible confounding effects in RSFC without introducing artifactual biases in the estimated connectivity measures.

In addition to physiological artifacts, head motion artifacts have been shown to significantly influence intrinsic functional connectivity measurements (Satterthwaite et al., 2012; Van Dijk et al., 2012). Moreover, it has been recently demonstrated that artifacts in the functional time series may result in substantial changes in RSFC data despite standard compensatory regression of motion estimates from the data (Power et al., 2012). These findings suggest that rigorous artifact rejection in addition to motion regression is especially prudent for valid interpretation of RSFC. *Conn* is seamlessly interoperable with quality assurance and artifact rejection software, *art* (www.nitrc.org/projects/artifact_detect/), such that a matrix of outlier, artifactual time points saved by *art* may be easily entered as first-level covariates in *Conn*. The combination of the *Conn*'s implementation of the CompCor method of noise reduction along with the efficient rejection of motion and artifactual time points allows for better interpretation of functional connectivity results for both correlated and anti-correlated networks.

With the increase in popularity of linear functional connectivity analysis, there is still a large degree of variability in the exact methods used for the analysis of fcMRI data, with differences in noise-preprocessing steps as well as differences in the characterization of fcMRI measures across labs, which can complicate the interpretation and comparison of fcMRI results across different studies. To provide a common framework for the analysis of fcMRI data, we have developed and made publicly available the *Conn* toolbox (www.nitrc.org/projects/conn). The toolbox is compatible with most data formats—including nifty (nii) and analyze images (img)—and implements all the processing steps necessary to perform fcMRI analysis—including spatial preprocessing of BOLD signal and anatomical volumes, CompCor removal of noise sources, first-level estimation of fcMRI measures, and second-level random effect analysis—while maintaining the flexibility to define and estimate different forms of fcMRI analysis. The implementation includes standard fcMRI analysis, such as estimation of seed-to-voxel and ROI-to-ROI functional correlations, as well as other forms of fcMRI analysis, such as bivariate regression analysis, semipartial correlation and multivariate regression analysis of multiple ROI sources, graph theoretical analysis of brain networks, and novel voxel-to-voxel analysis of functional connectivity. In the following sections we first describe in detail the methods used by the toolbox to compute different functional connectivity measures (Functional Connectivity Metrics in *Conn* section), and then we illustrate examples of use and reliability estimates of all of these fcMRI measures indicating their validity as potentially useful neuromarkers (Illustration of Functional Connectivity Analysis in *Conn* section).

Functional Connectivity Metrics Implemented in *Conn*

The analysis steps involved in the computation of fcMRI measures, as implemented in the *Conn* toolbox, are illustrated in Figure 1. The following sections explain these steps in detail.

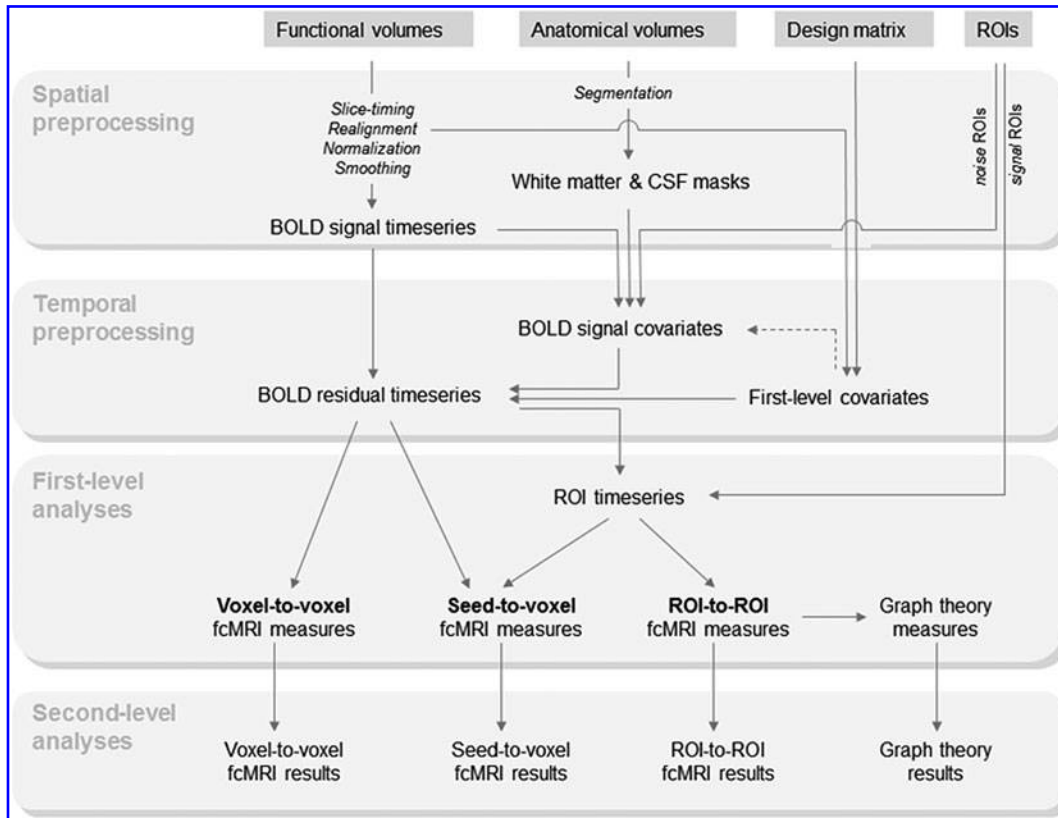


FIG. 1. Schematic representation of fcMRI analysis steps. BOLD, blood oxygen level-dependent; CSF, cerebrospinal fluid; fcMRI, functional connectivity magnetic resonance imaging; ROI, region of interest.

Spatial preprocessing

Spatial preprocessing steps for functional connectivity analysis do not typically differ from those used in the context of functional activation analysis. Most fcMRI studies include slice-timing correction, realignment, coregistration and/or normalization, and spatial smoothing. In addition to these steps, the toolbox employs segmentation of gray matter, white matter, and cerebrospinal fluid (CSF) areas for optional use during removal of temporal confounding factors. All spatial preprocessing steps are implemented using SPM8 (Wellcome Department of Imaging Neuroscience, London, UK; www.fil.ion.ucl.ac.uk/spm); however, users can choose to omit this step and use their own spatial preprocessing pipeline.

Temporal processing (treatment of temporal confounding factors)

Several studies have emphasized the importance of additional preprocessing steps in fcMRI studies (e.g., Birn et al., 2006; Fox et al., 2005, 2009; Power et al., 2012; Van Dijk et al., 2010; Weissenbacher et al., 2009), including—but not limited to—band-pass filtering and the inclusion of estimated subject motion parameters, artifacts, respiratory and cardiac signals, global BOLD signal, and BOLD signals in white matter and CSF areas as additional covariates. The main concern is that movement and physiological noise sources can potentially induce spurious correlations among distant voxels, increasing the chance of false positives and confounding the interpretation of fcMRI results. These additional preprocessing steps are designed to help mitigate the impact of motion and physiological noise factors, increasing the validity and the robustness of fcMRI analysis.

The toolbox allows the specification of an arbitrary set of possible temporal confounding factors, which can be defined from indirect sources, as subject- and session-specific time series (e.g., estimated subject movement parameters and artifacts, cardiac or respiratory rates, and possible task effects; these are indicated in Figure 1 as *Design matrix*), as well as BOLD signals obtained from subject-specific noise ROIs (white matter and CSF masks, as well as optionally additional user-defined ROIs). The toolbox implements an anatomical aCompCor strategy (Behzadi et al., 2007) in which a user-defined number of orthogonal time series are estimated using principal component analysis (PCA) of the multivariate BOLD signal within each of these noise ROIs. This strategy generalizes the common practice of extracting the average BOLD time series from one or several seeds located within the white matter and/or CSF areas. In addition, and for each original temporal confounding factor, first- and higher-order derivatives of the associated time series can also be defined by the user as additional confounding factors (e.g., Fox et al., 2005). Each of the defined temporal confounding factors is then regressed from the BOLD time series at each voxel (separately for each session), and the resulting residual time series are band-pass filtered. In particular, the removal of temporal confounding factors, from an observed signal $BOLD^*(v,t)$ at voxel v and time t , takes the following form:

$$\begin{aligned}
 BOLD(v,t) = & BOLD^*(v,t) - \sum_{n=1}^N \hat{a}_n(v) \cdot c_n(t) \\
 & - \sum_{k=1}^K \sum_{n=1}^{M_k} \hat{b}_{kn}(v) \cdot d_{kn}(t)
 \end{aligned} \tag{1}$$

where $c_n(t)$ represents N temporal confounds defined explicitly through subject- and session-specific time series or implicitly as temporal derivatives of these signals (e.g., subject motion parameters); $d_{kn}(t)$ represents those confounds defined implicitly from K noise ROIs, each characterized by M_k component time series from each noise ROI (e.g., average signal, principal components, or temporal derivatives of these signals within white matter and CSF areas); and $a_n(v)$ and $b_{kn}(v)$ represent voxel-specific weights for each of these factors estimated using linear regression (see Appendix A.1 for further details of these preprocessing steps).

The toolbox graphical user interface (GUI) encourages users to explore the effect of these additional preprocessing steps by displaying the histogram of voxel-to-voxel functional connectivity values (correlation coefficients between the BOLD time series of a random subset of voxels) before and after regression of the selected temporal confounding factors. This display typically shows a heavily skewed distribution of connectivity values in the presence of motion and/or physiological noise sources, which is approximately centered and normalized by the regression process (Fig. 2). This exploration can help users optimize the choice of preprocessing steps as well as help detect anomalous subjects/sessions.

ROI time series

Functional connectivity measures are typically computed either between every pair of voxels (voxel-to-voxel analysis), between a seed voxel or area and every other voxel (seed-to-voxel analysis), or between each pair of seed areas (ROI-to-ROI analysis). The toolbox allows the definition of seed areas using standard practices, including individual mask image volumes [where an ROI is defined by all voxels with values above zero, e.g., WFU pickatlas files (Maldjian et al., 2003) or functional mask files defined using SPM *save* func-

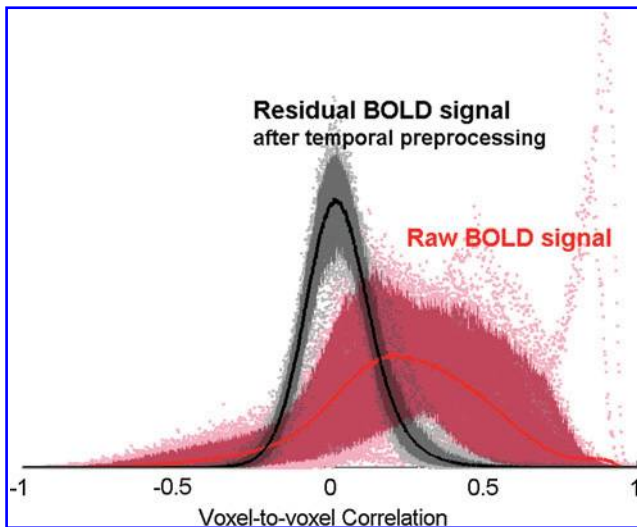


FIG. 2. Effect of temporal preprocessing steps on the distribution of voxel-to-voxel BOLD signal correlation values. The average distribution (across subjects and sessions) is shown as thick lines, and its 5% and 95% percentiles are shown as filled areas. After temporal preprocessing, voxel-to-voxel functional connectivity estimates show a reduction in bias and an associated increase in reliability across subjects and sessions (see text for details).

tionality], text files (listing Montreal Neurological Institute (MNI) coordinates of ROI voxels), and atlas image volumes where multiple ROIs can be jointly defined using a single image volume. Each ROI is characterized by voxels sharing the same identifier number, for example, talairach atlas (Lancaster et al., 2000). ROIs can be defined separately for each subject (subject-specific ROIs) or jointly across all subjects (e.g., MNI space).

The average BOLD time series is computed across all the voxels within each ROI. In addition, the toolbox allows the extraction of additional temporal components from each area resulting from a principal component decomposition of the temporal covariance matrix (as for the noise ROIs above), as well as the estimation of higher-order temporal derivatives of these original BOLD signals. In general the following ROI time series can be computed from each seed area:

$$x_{n,m}(t) = \sum_{v \in \Omega_s} w_m(v) \cdot \frac{\partial^n}{\partial t^n} \text{BOLD}(v, t) \quad (2)$$

$\text{BOLD}(v, t)$: BOLD timeseries at voxel v and time t

Ω_s : voxels in seed area

m : order of PCA component (0 for straight average)

n : order of temporal derivative (0 for original signal)

In combination with the average BOLD signal within an ROI, PCA component signals allow multivariate analysis of functional connectivity patterns. In addition, temporal derivative BOLD signals when used in combination with multivariate measures of connectivity (e.g., multivariate regression or semipartial correlation measures) allow the exploration of temporal lags or more complex linear dynamics between two areas.

Linear fcMRI measures

The toolbox focuses on linear measures of functional connectivity between two sources: zero-lagged *bivariate-correlation* and *bivariate-regression* coefficients, and their associated multivariate measures, *semipartial-correlation* and *multivariate-regression* coefficients (Table 1). Bivariate correlation and regression coefficients measure the level of linear association of the BOLD time series between each pair of sources when considered in isolation. In contrast, semipartial correlation and multivariate regression coefficients consider multiple sources simultaneously and estimate the unique contribution of each source using a general linear model. In bivariate and semipartial correlation analyses, effect sizes represent correlation coefficients (their values squared can be interpreted as the percentage of the target BOLD signal variance explained by each source BOLD signal). In bivariate and multivariate regression analyses, effect sizes represent %

TABLE 1. DEFINITION OF LINEAR MEASURES OF FUNCTIONAL CONNECTIVITY

Bivariate regression	$b = (x^t \cdot x)^{-1} \cdot (x^t \cdot y)$
Bivariate correlation	$r = (x^t \cdot x)^{1/2} \cdot b \cdot (y^t \cdot y)^{-1/2}$
Multivariate regression	$B = (X^t \cdot X)^{-1} \cdot (X^t \cdot Y)$
Semipartial correlation	$R = [(X^t \cdot X)^{-1}]^{-1/2} \cdot B \cdot [Y^t \cdot Y]^{-1/2}$

x and y represent two BOLD time series vectors (centered), X and Y represent matrices created by concatenating horizontally one or several x and y vectors, and the brackets $[\]$ represent the operation of zeroing all the nondiagonal elements in a matrix.

changes in BOLD activity at each target associated with a 1% change of BOLD activity at each source ROI. Before being entered into second-level between-subjects analysis, a Fisher transformation (inverse hyperbolic tangent function) is applied to all bivariate and semipartial correlation measures in order to improve the normality assumptions of standard second-level general linear models.

Voxel-to-voxel measures

The toolbox also computes a complete voxel-to-voxel functional correlation matrix for each subject. From the residual BOLD time series at every voxel within an a priori gray matter mask (isotropic 2-mm voxels), the matrix of voxel-to-voxel bivariate correlation coefficients is computed. To minimize storage and computation requirements (explicit storage of this matrix could occupy above 300 Gb for each subject), this matrix is instead characterized without loss of precision by its eigenvectors and associated eigenvalues (see Appendix A.2). In addition to downsampling the voxel-to-voxel correlation matrices to any desired target resolution, the toolbox also computes several voxel-level measures of functional connectivity directly from the original voxel-to-voxel correlation matrix (see Table 2). Integrated local correlation (ILC) (Deshpande et al. 2007) characterizes the average local connectivity between each voxel and its neighbors. Radial correlation contrast (RCC) (Goelman, 2004) characterizes the spatial asymmetry of the local connectivity pattern between each voxel and its neighbors. Intrinsic connectivity contrast (ICC) (Martuzzi et al. 2011) and radial similarity contrast (RSC) (Kim et al., 2010) are novel measures similar to ILC and RCC measures, but characterizing the global connectivity pattern between each voxel and the rest of the brain (instead of the local connectivity pattern around each voxel). In particular, ICC characterizes the strength of the global connectivity pattern between each voxel and the rest of the brain, while RSC characterizes the global similarity between the connectivity patterns of neighboring voxels. In addition to these measures the toolbox allows simple and fast implementation of other user-defined voxel-level fcMRI measures, as long as these measures can also be characterized as a function of the eigenvectors/eigenvalues of the voxel-to-voxel correlation matrix.

TABLE 2. VOXEL-LEVEL FUNCTIONAL CONNECTIVITY MRI MEASURES DERIVED FROM THE VOXEL-TO-VOXEL CONNECTIVITY MATRIX $r(x,y)$

Integrated local correlation	$\sum_{y \in \Omega} h_{\sigma}(x-y) \cdot r(x,y)$
Radial correlation contrast	$\sum_{y \in \Omega} h_{\sigma}(x-y) \cdot \frac{\partial}{\partial x_k} r(x,y)$
Global correlation strength	$\frac{1}{ \Omega } \sum_{y \in \Omega} r(x,y) ^2$
Radial similarity contrast	$\frac{1}{ \Omega } \sum_{y \in \Omega} \left \frac{\partial}{\partial x} r(x,y) \right ^2$

Integrated local correlation and radial correlation contrast characterize properties of the local pattern of connectivity (between each voxel and its neighbors). Global correlation strength and radial similarity contrast characterize properties of the global pattern of connectivity (between each voxel and the entire brain).

x and y represent the spatial locations of two arbitrary voxels, h_{σ} represents a Gaussian convolution kernel of width σ , and Ω represents the set of all brain voxels.

The Illustration of Functional Connectivity Analysis in *Conn* section [Illustration of voxel-to-voxel analysis (optimal placement of fcMRI seeds) subsection] illustrates the application of one such user-defined measure to investigate between-session similarity of functional connectivity patterns, and Appendix A.2 describes the characterization of this measure as a function of the eigenvectors/eigenvalues of the voxel-to-voxel connectivity matrix.

Task-related and resting state fcMRI

The previous sections characterize the steps necessary to perform first-level (within-subjects) connectivity analysis of resting state BOLD time series, as well as time series derived from the residuals of BOLD time series in block- and event-related designs after removing modeled task or condition effects (Fair et al., 2007) (e.g., simply by including these modeled condition effects as additional temporal confounding factors). The toolbox also allows condition-dependent functional connectivity analysis of block design studies, such as fcMRI analysis of interleaved resting periods or analysis of functional connectivity within task blocks. In these cases and after the session-specific treatment of temporal confounds, the BOLD time series is divided into scans associated with each blocked presentation. To take into account the hemodynamic delay, block regressors for each condition are convolved with a canonical hemodynamic response function, a combination of two gamma functions, and rectified {filtered to keep the positive part of the original time series; $y[n] = \max(0, x[n])$ }. All of the scans with nonzero effects in the resulting time series are concatenated for each condition and across all sessions, weighting each scan by the value of these time series. Alternatively it is also possible to use a Hann function (e.g., a ‘‘Hann function’’ window, shaped as a half cycle of a sine-squared function) instead of the rectified hrf function that more heavily de-weights the scans at the beginning and end of each block, as well as to omit any form of within-block weighting. In the case of block design studies, it is also recommended to include standard task regressors (block regressors convolved with a canonical hemodynamic response function) and their first-derivative terms as additional covariates in the temporal preprocessing step. This step helps avoid possible between-condition main effects from affecting within-condition connectivity estimates in the presence of possible voxel-specific differences in hemodynamic delay. Resting state analysis is treated like a special case of task-specific analysis where only one condition spanning the entire scanner acquisition length is considered.

Second-level analysis

Following the computation for each subject of seed-to-voxel connectivity maps, ROI-to-ROI connectivity matrices, and voxel-level fcMRI measures from voxel-to-voxel analysis, each one of these measures can then be entered into a second-level general linear model to obtain population-level estimates and inferences. Specific hypotheses can then be tested using between-subjects contrasts (e.g., comparing functional connectivity patterns between two groups of subjects), between-condition contrasts (e.g., comparing task- or condition-specific connectivity patterns between two conditions), between-source contrasts (e.g., comparing functional connectivity

patterns between two seeds), and combinations of these contrasts (e.g., testing group by condition interactions). False positive control in ROI-to-ROI analysis is implemented using uncorrected or false discovery rate (FDR)-corrected p -values. Uncorrected p -values are appropriate when the researcher's original hypotheses involve only the connectivity between two a priori ROIs and FDR-corrected p -values are appropriate when the researcher's original hypotheses involve the connectivity between larger sets of ROIs and do not specify a priori which ROIs are expected to show an effect. False positive control in voxel-level analysis is implemented through a combination of a voxel-level height threshold (defined by uncorrected or FDR-corrected voxel-level p -values) and a cluster-level extent threshold (defined by uncorrected, family wise error [FWE]-corrected, or FDR-corrected cluster-level p -values).

Graph theoretical analysis

The toolbox also computes several graph theoretical measures (Achard and Bullmore, 2007; Bullmore and Sporns, 2009; Latora and Marchiori, 2001; Watts and Strogatz, 1998) characterizing structural properties of the estimated ROI-to-ROI functional connectivity networks, and allows users to perform group-level analysis of these measures. Each subject-specific ROI-to-ROI connectivity matrix is thresholded at a fixed level. This threshold can be based on raw connectivity values, normalized z-scores, or percentile scores (resulting in graphs with fixed network-level cost). Suprathreshold connectivity values define an adjacency matrix characterizing a graph with nodes associated with ROIs, and edges associated with the strength of functional connectivity among these ROIs. For each node n in a graph G , $cost$ is defined as the proportion of connected neighbors, $global\ efficiency$ is defined as the average inverse shortest path distance from node n to all other nodes in the graph, and $local\ efficiency$ is defined as the average global efficiency across all nodes in the local subgraph of node n (the subgraph consisting only of nodes neighboring node n). In addition, equivalent network-level summary measures can be defined by averaging across all nodes of the network (Table 3). Population-level inferences on these graph theoretical measures are obtained using a second-level general linear model as in the fcMRI analysis above.

Illustration of Functional Connectivity Analysis in Conn

In this section several examples of fcMRI analysis performed with *Conn* are illustrated. These examples are chosen to illustrate some of the standard approaches available for RSFC analysis, as well as to demonstrate the reliability of

the functional connectivity measures computed by the *Conn* toolbox. The analyses were based on a publically available resting state dataset (NYU CSC TestRetest dataset, www.nitrc.org/projects/nyu_trt), which has been previously analyzed in detail demonstrating the reliability of functional connectivity measures (Shehzad et al., 2009). This dataset consists of echo planar imaging (EPI) images of 25 participants collected on three occasions: (1) the first resting state scan in a scan session, (2) 5–11 months after the first resting state scan, and (3) about 30 (<45) min after the second resting state scan. Resting state scans consist of 197 continuous EPI functional volumes (TR=2000 ms; TE=25 ms; flip angle=90; 39 slices, matrix=64×64, FOV=192 mm; isotropic 3-mm acquisition voxel size).

Preprocessing of BOLD time courses

Spatial preprocessing of functional volumes included realignment, normalization, and smoothing (8-mm FWHM Gaussian filter), using SPM8 default parameter choices. Anatomical volumes were segmented into gray matter, white matter, and CSF areas, and the resulting masks were eroded (one voxel erosion, isotropic 2-mm voxel size) to minimize partial volume effects. The temporal time series characterizing the estimated subject motion (three-rotation and three-translation parameters, plus another six parameters representing their first-order temporal derivatives), as well as the BOLD time series within the subject-specific white matter mask (three PCA parameters) and CSF mask (three PCA parameters), were used as temporal covariates and removed from the BOLD functional data using linear regression, and the resulting residual BOLD time series were band-pass filtered (0.01 Hz < f < 0.10 Hz). Figure 2 illustrates the effect of removing temporal covariates on the distribution of voxel-to-voxel BOLD signal correlation values. A random subset of 256 voxels (the same voxels across subjects and sessions) was used to compute the sample distribution of voxel-to-voxel BOLD signal correlation values separately for each subject and session, before and after removal of the defined temporal covariates.

Estimated voxel-to-voxel correlations using the raw BOLD signals typically show distributions with some degree of positive bias, and with large differences between sessions and subjects. In contrast, after temporal preprocessing, the estimated voxel-to-voxel correlations appear more centered and with very similar distributions across sessions and subjects. To quantify this observation, we computed measures of inter-session reliability of the voxel-to-voxel connectivity measures from the raw BOLD signal, and compared them with the

TABLE 3. DEFINITION OF GRAPH THEORETICAL MEASURES CHARACTERIZING STRUCTURAL PROPERTIES OF FUNCTIONAL CONNECTIVITY NETWORKS

	ROI-level measures	Network-level measures
Cost	$C_n(G) = \frac{1}{ G - 1} \cdot G_n $	$C(G) = \frac{1}{ G } \cdot \sum_{n \in G} C_n(G)$
Global efficiency	$E_n^{global}(G) = \frac{1}{ G - 1} \cdot \sum_{m \neq n \in G} d_{nm}^{-1}(G)$	$E^{global}(G) = \frac{1}{ G } \cdot \sum_{n \in G} E_n^{global}(G)$
Local efficiency	$E_n^{local}(G) = E_n^{global}(G_n)$	$E^{local}(G) = \frac{1}{ G } \cdot \sum_{n \in G} E_n^{local}(G)$

$d_{nm}(G)$ represents the shortest path distance between nodes n and m in graph G , and $|G|$ represents the number of nodes in graph G . ROI, region of interest.

same measures after temporal preprocessing. The reliability (average intersession correlation) of the resulting group-level voxel-to-voxel connectivity estimates between randomly selected voxels was $r=0.52$ from the raw BOLD signal, $r=0.62$ when using subject motion covariates, and $r=0.70$ when additionally using CompCor method of white matter and CSF noise covariates, and their corresponding intraclass correlation coefficients (one-way random effects, Shehzad et al. 2009) were 0.22, 0.55, and 0.71, respectively. These results highlight that reliability of group-level voxel-to-voxel connectivity measures increases dramatically with the additional methods of noise reduction implemented in the temporal preprocessing steps of the *Conn* toolbox, potentially due to their effect reducing physiological and other noise-dependent biases on functional connectivity estimates.

Illustration of seed-to-voxel bivariate correlation analysis

A posterior cingulate cortex (PCC) region [a spherical ROI with MNI coordinates $(-6, -52, 40)$ and radius 10 mm (Fox et al., 2005)] was used as the seed. The PCC seed shows positive functional connectivity with a network of default areas

(shown in red in Fig. 3 top) and negative functional connectivity (shown in blue) with task-related regions. In addition, three separate within-session estimates of the connectivity strength between the PCC seed and each voxel were computed. These session-specific estimates represent the Fisher-transformed correlation coefficients for each voxel averaged across all subjects and converted back to raw correlation coefficient values. Within-session estimates (Fig. 3) show a high degree of reliability (intersession correlation $r=0.95$, mean absolute error 0.03) when comparing group-level estimates of functional connectivity strength across repeated runs or sessions. Similarly, high interscan reliability ($r=0.97$) was found when repeating these analyses using bivariate regression measures instead of bivariate correlation measures.

Illustration of seed-to-voxel semipartial correlation analysis

Multivariate seed-to-voxel analysis was also performed to explore the unique connectivity with the PCC area that is not mediated by other default network areas. The average BOLD time series within the PCC area were used as sources of the

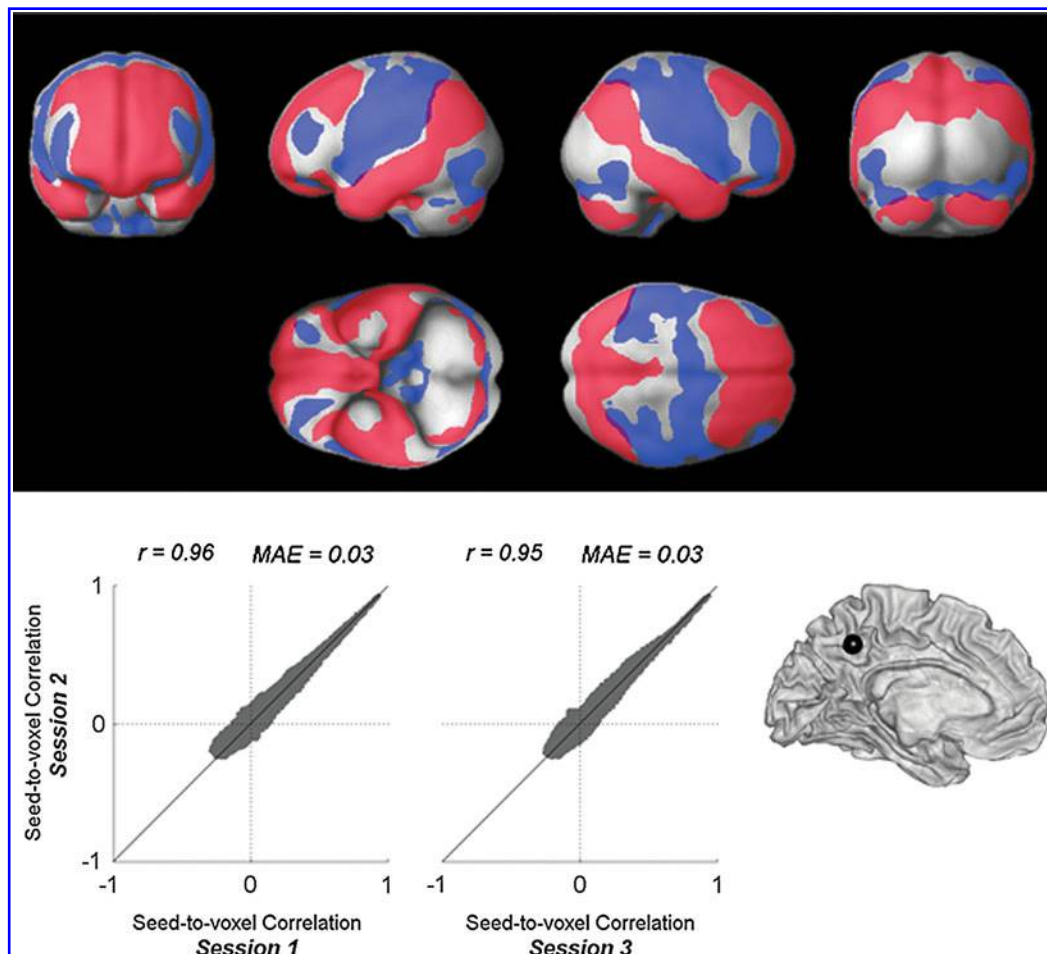


FIG. 3. Seed-to-voxel functional connectivity with PCC seed area. Top: Spatial patterns of group-level seed-to-voxel connectivity measures (bivariate correlation) collapsed across the three sessions available from each subject. Red: positive connectivity, blue: negative connectivity. Results are thresholded at FWE-corrected cluster-level $p < 0.05$ (with FDR-corrected two-sided $p < 0.05$ height threshold). Bottom: Intersession reliability. Correlations between session-specific estimates of group-level seed-to-voxel connectivity measures, between session 2 and session 1 (5–11-month difference between the sessions), and between session 2 and session 3 (30-min difference between the sessions). FWE, family wise error; FDR, false discovery rate; PCC, posterior cingulate cortex.

seed-to-voxel analysis. A multivariate representation of the activation within three control ROIs—medial prefrontal cortex (MPFC), left lateral parietal, and right lateral parietal—characterizing, for each ROI, the average BOLD activation plus four orthogonal components derived from a principal component decomposition of the within-ROI BOLD time series were used as control variables. Semipartial correlation values with the PCC seed were estimated for each voxel. PCC shows unique positive and negative functional connectivity with a large network of areas that are not mediated by other default network regions (Fig. 4). In addition, three separate within-session estimates of the semipartial correlation coefficients between the PCC seed and each voxel were computed. These session-specific estimates represent the Fisher-transformed semipartial correlation coefficients for each voxel averaged across all subjects and converted back to raw correlation coefficient values. Within-session estimates show a high degree of reliability (intersession correlation $r=0.82$, mean absolute error 0.03) when comparing group-level estimates of unique functional connectivity strength across repeated runs or sessions (Fig. 4). Similar interscan reliability ($r=0.88$) was found when repeating these analyses using multivariate regression measures instead of semipartial correlation measures.

Illustration of ROI-to-ROI analysis

This analysis uses the same PCC seed area as the previous seed-to-voxel analysis, and estimates the ROI-to-ROI functional connectivity (bivariate correlation measure) between this seed and a set of 84 ROIs defining the Brodmann areas (talairach atlas; Lancaster et al., 2000). Group-level estimates of ROI-to-ROI connectivity show a high degree of reliability (Fig. 5; intersession correlation $r=0.99$, mean absolute error 0.01). Similar interscan reliability ($r=0.98$) was found when repeating these analyses using bivariate regression measures instead of bivariate correlation measures.

Illustration of graph metrics analysis

The entire matrix of ROI-to-ROI functional connectivity values (bivariate correlation measure) was computed for each subject using the Brodmann area ROIs, and thresholded at a fixed network-level cost value to define an undirected graph characterizing the entire network of functional connections between these ROIs. Negative functional connectivity values were disregarded in these analyses. The network global and local efficiency was computed for a range of possible cost value (K) thresholds and compared to a random graph and to a lattice graph with the same network size

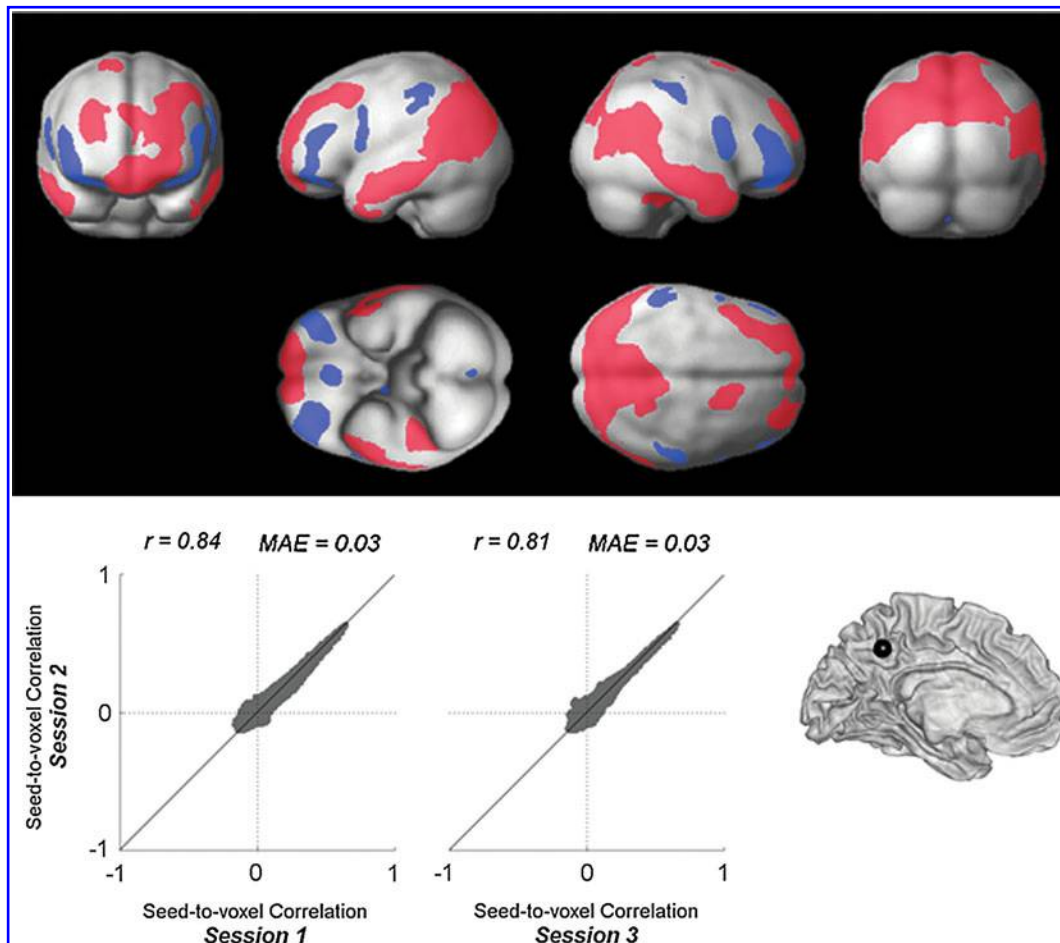


FIG. 4. Seed-to-voxel analysis of unique connectivity with PCC seed area (controlled by MPFC, left and right LP). Top: Spatial pattern of group-level effects of the semipartial correlation coefficients collapsed across the three sessions available from each subject. Results are thresholded at FWE-corrected cluster-level $p < 0.05$ (with FDR-corrected two-sided $p < 0.05$ height threshold). Bottom: Intersession reliability of semipartial correlation measures with PCC seed. MPFC, medial prefrontal cortex; LP, lateral parietal.

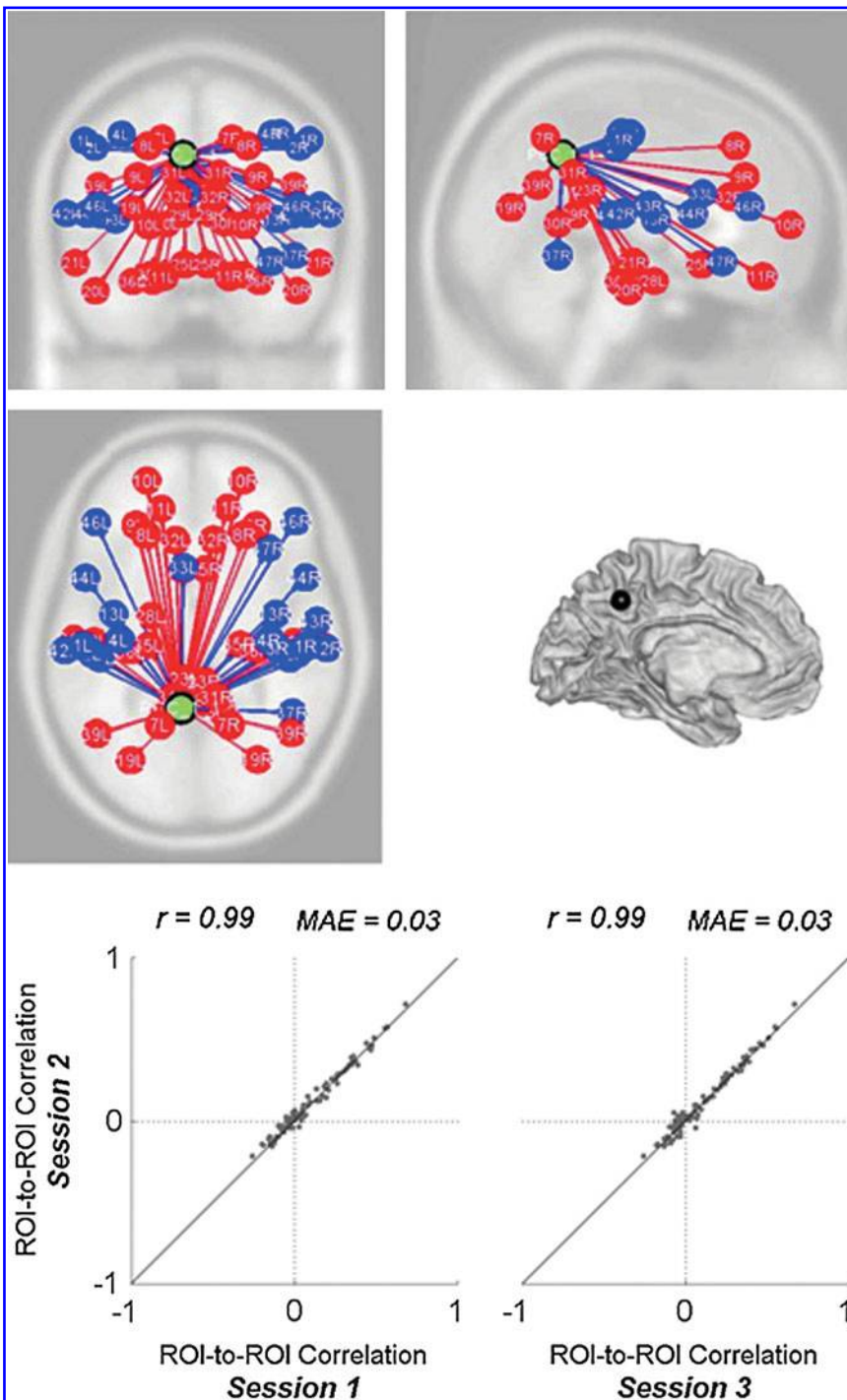


FIG. 5. ROI-to-ROI functional connectivity with PCC seed area. Top: ROIs defined from talairach atlas Brodmann areas that show positive (red) and negative (blue) functional connectivity with PCC are shown (for display clarity each ROI is identified by its centroid positions). Results are thresholded at FDR-corrected $p < 0.05$. Bottom: Intersession reliability of ROI-to-ROI group-level functional connectivity measures.

and cost (Fig. 6). Small world properties were observed in the range of costs $0.05 < K < 0.25$, where global efficiency is greater than that of a lattice graph and local efficiency is greater than that of a random graph (Achard and Bullmore, 2007). Using an intermediate $K=0.15$ cost threshold level, the global efficiency of each ROI, a measure of the centrality of each ROI within the network, was computed and averaged across all subjects. This measure showed a high degree of reliability when comparing session-specific estimates of global efficiency across repeated runs or sessions (Fig. 6; intersession correlation $r=0.95$, mean absolute error 0.01). Similar inter-

scan reliability was found for other graph theoretical measures (local efficiency $r=0.90$; cost $r=0.95$).

Illustration of voxel-to-voxel analysis (RSC)

This analysis investigates the similarity, at each voxel, between the global functional connectivity patterns of this voxel and those of its neighbors. The voxel-to-voxel functional connectivity matrix was computed separately for each session using an isotropic 2-mm voxels within an a priori gray matter mask (SPM apriori/grey.nii mask thresholded at

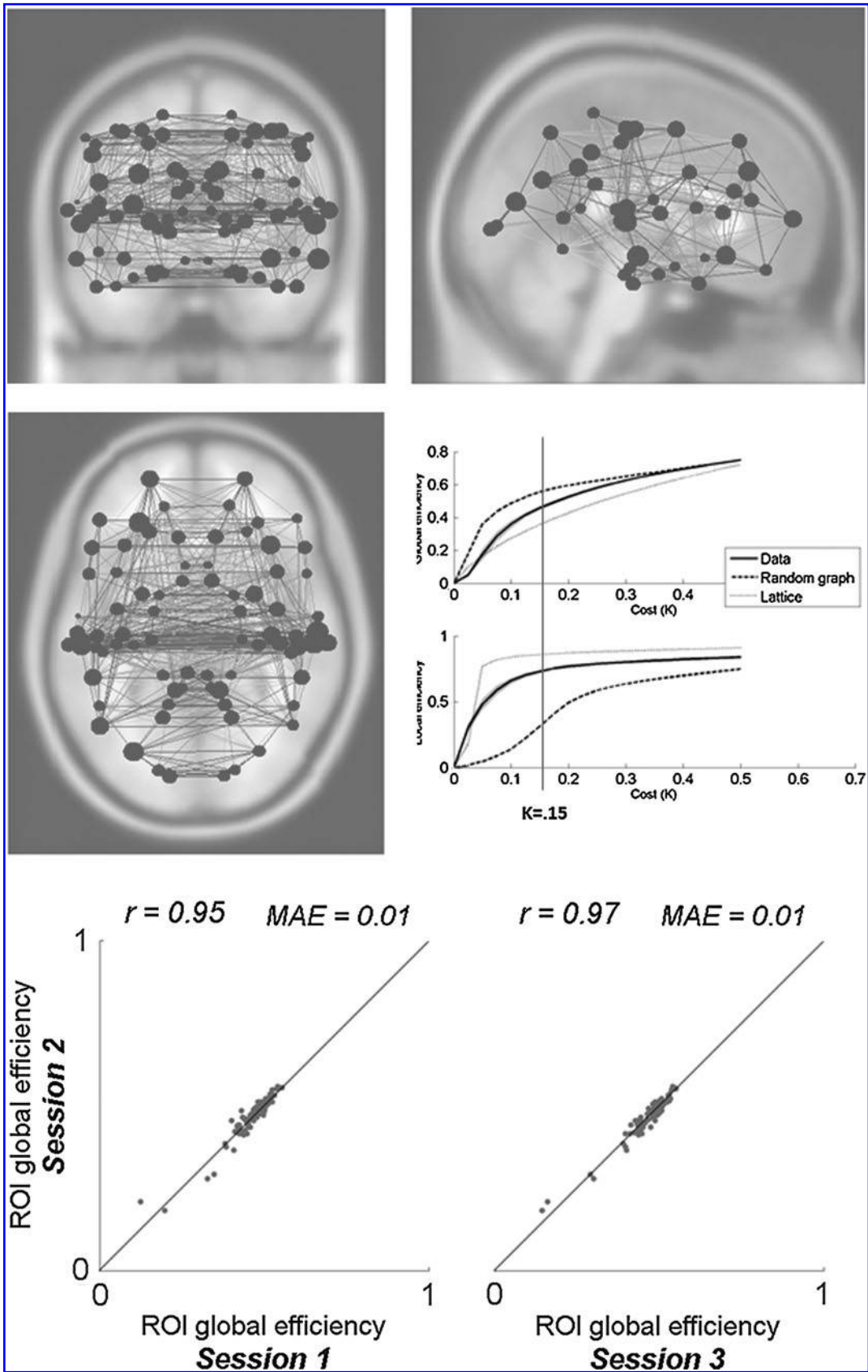


FIG. 6. ROI-level analysis of global efficiency. Top: Global efficiency of each ROI (a measure of ROI centrality, and shown proportional to circle sizes in the left display) in the network defined by positively associated ROIs (ROIs defined from talairach atlas Brodmann areas). Small world properties, where global efficiency is greater than that of a lattice graph and local efficiency is greater than that of a random graph, are observed at the chosen cost threshold level ($K=0.15$). Bottom: Intersession reliability of the estimated group-level measures of global efficiency for each ROI.

$p > 0.25$; $N = 212,792$ voxels). The RSC measure computes the norm of the difference between the functional connectivity patterns (rows of the voxel-to-voxel matrix) of neighboring voxels. Average group-level RSC across all sessions is shown in Figure 7 (top). Within-session estimates (Fig. 7 bottom) show a high degree of reliability (intersession correlation $r = 0.98$, mean absolute error 0.002) when comparing group-level estimates of RSC across repeated runs or sessions. Similar interscan reliability was found for other voxel-level fMRI measures derived from voxel-to-voxel analysis (ILC $r = 0.98$; RCC $r = 0.99$; GCS $r = 0.97$).

Illustration of voxel-to-voxel analysis (optimal placement of fMRI seeds)

This analysis investigates the reliability of seed-to-voxel functional connectivity estimates across all possible seed locations. They were implemented as voxel-to-voxel analysis using a user-defined measure characterizing the between-session similarity of functional connectivity patterns at each voxel. Isotropic 2-mm voxels within an a priori gray matter mask (SPM apriori/grey.nii mask thresholded at $p > 0.25$) were used for this analysis ($N = 212,792$ voxels). The matrix of voxel-to-voxel functional connectivity values (bivariate correlation matrix, with size $N \times N$) was parameterized separately for each subject and for each session (Appendix A.2). Separately for each row of this matrix (subject-specific functional connectivity estimates between a given seed voxel and all of the gray matter voxels) the intersession correlation was computed and averaged across each pair of sessions and

across all subjects. The resulting measures (for each voxel) characterize the average subject-level intersession reliability of seed-to-voxel analysis when using each voxel as a possible seed location (c.f. group-level reliability measure used in the previous sections) (Fig. 8). Intersession reliability values of subject-level connectivity estimates ranged between $r = 0.01$ and $r = 0.62$ (average $r = 0.29$) across all possible seed locations. Local peaks in this map characterize optimal seed locations (they result in seed-to-voxel functional connectivity patterns that are more robust across sessions than those patterns resulting when using neighboring seed locations). Peak values with intersession reliability above $r = 0.50$ are shown in Figure 8 (bottom). Robust seed locations were identified in default network areas—PCC, MPFC, and lateral parietal—in close agreement with standard seed locations for these areas (Fox et al., 2005). In addition, other robust locations included superior temporal gyrus (one anterior temporal source, and a different posterior source close to supramarginal gyrus), superior frontal gyrus, and cingulate gyrus. The results showed high degree of hemispheric symmetry, with all of the peaks (except medial peaks: MPFC, PCC, and cingulate gyrus) having a corresponding peak with similar location and reliability in the opposite hemisphere. Since the seed with highest reliability ($0, -56, 28$) was close but slightly inferior to the a priori PCC seed location used in the previous sections ($-6, -52, 40$), we defined for comparison a new seed location using a spherical ROI of 10 mm centered at the new coordinates ($0, -56, 28$). The group-level and subject-level intersession reliability of the seed-to-voxel functional connectivity estimates when using this new seed definition was $r = 0.97$ and

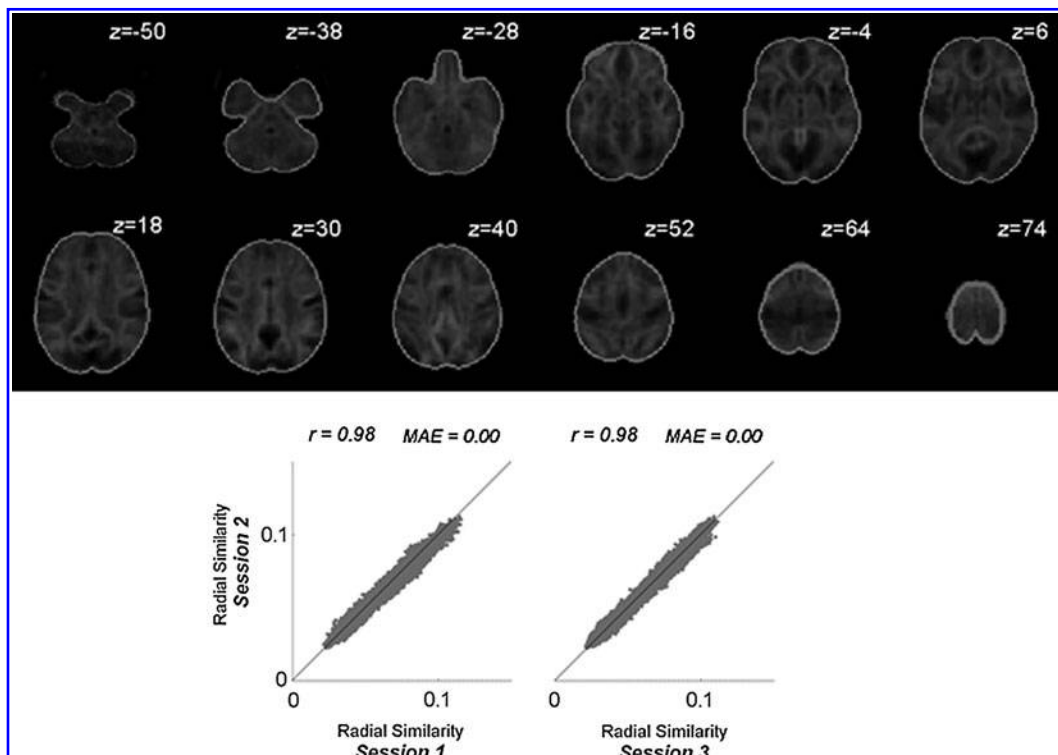


FIG. 7. Voxel-to-voxel analysis of radial similarity contrast measure. Top: Average group-level radial similarity contrast at each voxel. Darker shades for a voxel indicate higher similarity between the global functional connectivity patterns of this voxel and those of its neighbors. Bottom: Intersession reliability of the group-level radial similarity contrast measure.

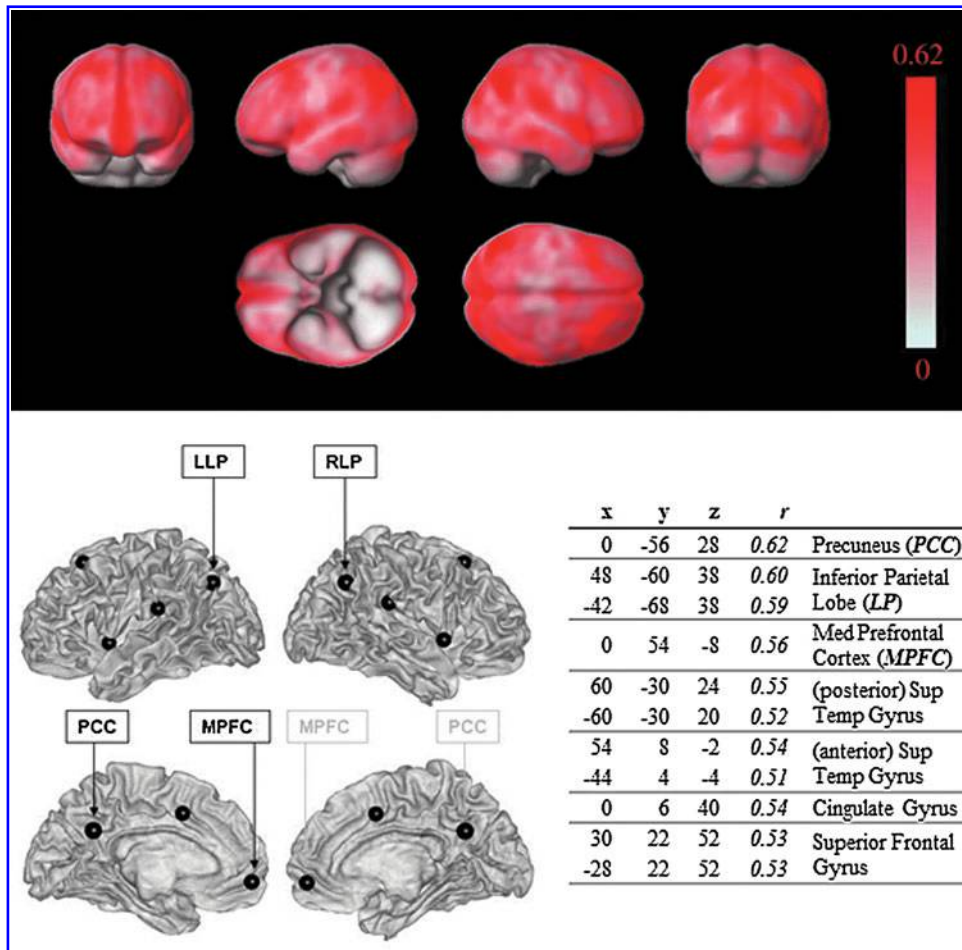


FIG. 8. Voxel-to-voxel analysis studying robustness of seed locations. Top: Intersession reliability maps. This display shows the intersession correlation between functional connectivity patterns for all possible seed locations. Darker shades for a voxel indicate that this voxel, when used as seed for standard seed-to-voxel functional connectivity analysis, results in connectivity patterns that are better replicated across sessions (higher intersession correlations). Bottom: Optimal seed locations, as estimated from the local peaks of the reliability maps above. Seed locations that show local maxima in reliability when comparing subject-level estimates of functional connectivity strength across repeated runs or sessions (r value represents the subject-specific intersession correlation averaged across all subjects). All seeds with average $r > 0.50$ are shown. Peak locations are reported as (x,y,z) Montreal Neurological Institute coordinates. LLP, left lateral parietal; RLP, right lateral parietal.

$r=0.64$, respectively (compared with $r=0.95$ and $r=0.55$, respectively, when using the original *PCC* definition).

Discussion

RSFC analysis offers an important characterization of functional brain connectivity for both normal and patient populations. This article describes the methods used to compute a variety of functional connectivity measures in the *Conn* toolbox and illustrates the interscan reliability of these measures. The *Conn* toolbox offers a large suite of connectivity analyses packaged in a user-friendly GUI. The toolbox can be best used in conjunction with SPM but it is compatible with other analysis packages. The output of most processing and analysis procedures are stored as NIFTI volumes (e.g., the time series post noise reduction and correlation and Z-maps from seed voxel analysis) that may be used for further interrogation. For example, researchers may enter the subject-level Z-maps (Fisher-transformed subject-level correlation coefficients when performing bivariate-correlation analysis) in their anal-

ysis package of choice for additional second-level analysis. The toolbox also offers a complete batch processing environment facilitating the implementation of scalable and robust functional connectivity analysis using a simple common framework. In addition, the toolbox encourages users to explore their data at intermediate steps of the analyses (e.g., distribution of voxel-to-voxel connectivity estimates, spatial patterns of potential confounder effects, and individual subject-level connectivity maps), which can aid in detecting and correcting potential anomalies in the data as well as identifying sources of variability that might go unnoticed when focusing on group-level summary results alone.

Anticorrelations

There has been a debate as to whether observed anticorrelations are valid neurophysiological findings or analytic artifacts introduced by global signal regression, a common technique in removing confounds due to physiological and other noise sources in the BOLD time series (Buckner et al.,

2008; Fox et al., 2009; Murphy et al., 2009; Weissenbacher et al., 2009). There is general agreement, however, as may be illustrated with mathematical proof, that a seed voxel analysis using global signal regression will necessarily show anticorrelations even if none were truly present in the data because after global regression the distribution of the correlation coefficients between a voxel and every other voxel in the brain is shifted such that the sum ≤ 0 (Fox et al., 2009; Murphy et al., 2009). Because of this mathematical consequence of the shift in correlation distribution and because the global signal may contain important neural signals as well as noise, it has been recommended to refrain from interpreting anticorrelations when using global signal regression (Chang and Glover, 2009; Murphy et al., 2009).

However, the CompCor method of noise reduction, which does not rely on global signal regression or physiological monitoring, also results in anticorrelations, further supporting a biological basis for their existence, and the positive correlations have higher sensitivity and specificity than global signal regression (Chai et al., 2012). We believe that the CompCor method, as implemented in *Conn*, yields valid anticorrelations between large-scale brain networks.

Example illustrations

This article also describes the methods used to compute a variety of functional connectivity measures in the *Conn* toolbox and illustrates the interscan reliability of these measures. Seed-to-voxel and ROI-to-ROI measures of functional connectivity show high reliability for well-characterized seed locations in RSFC, both when using correlation- and regression-based measures to characterize functional connectivity. Similarly, graph theoretical measures characterizing structural properties of functional connectivity networks, as well as voxel-level measures characterizing the local connectivity patterns (between each voxel and its neighbors) and global connectivity patterns (between each voxel and the rest of the brain) also show high levels of interscan reliability.

Conclusions

The *Conn* toolbox offers a common framework to define and perform a large suite of connectivity analyses, including bivariate/semipartial correlations, bivariate/multivariate regression, seed-to-voxel connectivity, ROI-ROI connectivity, novel voxel-to-voxel connectivity, and graph theoretical measures for both resting state and task fMRI data. The analyses in this article show high levels of interscan reliability for a variety of fcMRI measures corroborating their potential application as useful neuromarkers. In addition, the *Conn* implementation of the anatomical CompCor method of noise reduction increases sensitivity and specificity of functional connectivity and allows for better interpretability of anticorrelations as it does not rely on global signal regression. We hope that the imaging community will benefit from the contribution of the tools.

Acknowledgments

The Poitras Center for Affective Disorders Research at the McGovern Institute for Brain Research at MIT supported this work. The authors thank Shay Mozes for initial programming support and John Gabrieli for comments on the article.

Author Disclosure Statement

The authors of the study have no conflict of interest to declare.

References

- Achard S, Bullmore E. 2007. Efficiency and cost of economical brain functional networks. *PLoS Comput Biol* 3:e17.
- Achard S, Salvador R, Whitcher B, Suckling J, Bullmore E. 2006. A resilient, low-frequency, small-world human brain functional network with highly connected association cortical hubs. *J Neurosci* 26:63–72.
- Aizenstein HJ, Butters MA, Wu M, Mazurkewicz LM, Stenger VA, Gianaros PJ, Becker TJ, Reynolds CF, Carter CS. 2009. Altered functioning of the executive control circuit in late-life depression: episodic and persistent phenomena. *Am J Geriatr Psychiatry: Off J Am Assoc Geriatr Psychiatry* 170:30–42.
- Behzadi Y, Restom K, Liu J, Liu TT. 2007. A component based noise correction method (CompCor) for BOLD and perfusion based fMRI. *NeuroImage* 37:90–101.
- Beckmann CF, DeLuca M, Devlin JT, Smith SM. 2005. Investigations into resting-state connectivity using independent component analysis. *Philos Trans R Soc Lond B Biol Sci* 360: 1001–1013.
- Beckmann CF, Mackay CE, Filippini N, Smith SM. 2009. Group comparison of resting-state fMRI data using multi-subject ICA and dual regression. *Neuroimage* 47:(Suppl. 1), S148.
- Birn RM, Diamon JB, Smith MA, Bandettini PA. 2006. Separating respiratory-variation-related fluctuations from neuronal-activity-related fluctuations in fMRI. *NeuroImage*, 31:1536–1548.
- Biswal B, Yetkin FZ, Haughton VM, Hyde JS. 1995. Functional connectivity in the motor cortex of resting human brain using echo-planar MRI. *Magn Reson Med* 34:537–541.
- Biswal BB, et al. 2010. Towards discovery science of human brain function. *Proc Natl Acad Sci* 107:4734–4739.
- Buckner RL, Andrews-Hanna JR, Schacter DL. 2008. The brain's default network: anatomy, function, and relevance to disease. *Ann N Y Acad Sci* 1124:1–38.
- Buckner RL, et al. 2009. Cortical hubs revealed by intrinsic functional connectivity: mapping, assessment of stability, and relation to Alzheimer's disease. *J Neurosci* 29:1860–1873.
- Bullmore E, Sporns O. 2009. Complex brain networks: graph theoretical analysis of structural and functional systems. *Nat Rev Neurosci* 10:186–198.
- Calhoun VD, Adali T, Pearlson GD, Pekar JJ. 2001. A method for making group inferences from functional MRI data using independent component analysis. *Hum Brain Mapp* 14:140–151.
- Calhoun VD, Adali T, Pekar JJ. 2004. A method for comparing group fMRI data using independent component analysis: application to visual, motor and visuomotor tasks. *Magn Reson Imaging* 22:1181–1191.
- Castellanos FX, Margulies DS, Kelly C, Uddin LQ, Ghaffari M, Kirsch A, Shaw D, Shehzad Z, Di Martino A, Biswal BB, Sonuga-Barke EJ, Rotrosen J, Adler LA, Milham MP. 2008. Cingulate-precuneus interactions: a new locus of dysfunction in adult attention-deficit/hyperactivity disorder. *Biol Psychiatry* 63:332–337.
- Chai XJ, Nieto-Castañón A, Öngür D, Whitfield-Gabrieli S. 2012. Anticorrelations in resting state networks without global signal regression. *Neuroimage* 59:1420–1428.
- Chang C, Glover GH. 2009. Effects of model-based physiological noise correction on default mode network anti-correlations and correlations. *NeuroImage* 47:1448–1459.

- Chen S, Ross TJ, Zhan W, Myers CS, Chuang KS, Heishman SJ, Stein EA, Yang Y. 2008. Group independent component analysis reveals consistent resting-state networks across multiple sessions. *Brain Res* 1239:141–151.
- Cohen AL, Fair DA, Dosenbach NU, Miezin FM, Dierker D, Van Essen DC, Schlaggar BL, Petersen SE. 2008. Defining functional areas in individual human brains using resting functional connectivity MRI. *NeuroImage* 41:45–57.
- Damoiseaux JS, Rombouts SA, Barkhof F, Scheltens P, Stam CJ, Smith SM, Beckmann CF. 2006. Consistent resting-state networks across healthy subjects. *Proc Natl Acad Sci U S A* 103:13848–13853.
- Deshpande G, LaConte S, Peltier S, Hu X. 2007. Integrated local correlation: A new measure of local coherence in fMRI data. *Hum Brain Mapp* 30:13–23.
- Di Martino A, Scheres A, Margulies DS, Kelly AM, Uddin LQ, Shehzad Z, Biswal B, Walters JR, Castellanos FX, Milham MP. 2008. Functional connectivity of human striatum: a resting state fMRI study. *Cereb Cortex* 18:2735–2747.
- Fair DA, Schlaggar BL, Cohen AL, Miezin FM, Dosenbach NU, Wenger KK, Fox MD, Snyder AZ, Raichle ME, Petersen SE. 2007. A method for using blocked and event-related fMRI data to study “resting state” functional connectivity. *NeuroImage* 35:396–405.
- Fox MD, Raichle ME. 2007. Spontaneous fluctuations in brain activity observed with functional magnetic resonance imaging. *Nat Rev Neurosci* 8:700–711.
- Fox MD, Snyder AZ, Vincent JL, Corbetta M, Van Essen DC, Raichle ME. 2005. The human brain is intrinsically organized into dynamic, anticorrelated functional networks. *Proc Natl Acad Sci U S A* 102:9673–9678.
- Fox MD, Snyder AZ, Zacks JM, Raichle ME. 2006. Coherent spontaneous activity accounts for trial-to-trial variability in human evoked brain responses. *Nat Neurosci* 9:23–25.
- Fox MD, Zhang D, Snyder AZ, Raichle ME. 2009. The global signal and observed anticorrelated resting state brain networks. *J Neurophysiol* 101:3270–3283.
- Fransson. 2005. Spontaneous low-frequency BOLD signal fluctuations: an fMRI investigation of the resting-state default mode of brain function hypothesis. *Hum Brain Mapp* 26:15–29.
- Fransson P, Skiold B, Horsch S, Nordell A, Blennow M, Lagercrantz H, Aden U. 2007. Resting-state networks in the infant brain. *Proc Natl Acad Sci U S A* 104:15531–15536.
- Friston KJ. 1994. Functional and effective connectivity in neuroimaging: a synthesis. *Hum Brain Mapp* 20:56–78.
- Friston KJ, Buechel C, Fink GR, Morris J, Rolls E, Dolan RJ. 1997. Psychophysiological and modulatory interactions in neuroimaging. *NeuroImage* 60:218–229.
- Friston KJ, Worsley KJ, Frackowiak RSJ, Mazziotta JC, Evans AC. 1994. Assessing the significance of focal activations using their spatial extent. *Hum Brain Mapp* 1:210–220.
- Fukunaga M, Horowitz SG, van Gelderen P, de Zwart JA, Jansma JM, Ikonomidou VN, Chu R, Deckers RH, Leopold DA, Duyn JH. 2006. Large-amplitude, spatially correlated fluctuations in BOLD fMRI signals during extended rest and early sleep stages. *Magn Reson Imaging* 24:979–992.
- Gitelman DR, Penny WD, Ashburner J, Friston KJ. 2003. Modeling regional and psychophysiological interactions in fMRI: the importance of hemodynamic deconvolution. *NeuroImage* 19:200–207.
- Goelman G. 2004. Radial correlation contrast—a functional connectivity MRI contrast to map changes in local neuronal communication. *Neuroimage* 23:1432–1439.
- Greicius MD, Flores BH, Menon V, Glover GH, Solvason HB, Kenna H, Reiss AL, Schlaggar AF. 2007. Resting-state functional connectivity in major depression: abnormally increased contributions from subgenual cingulate cortex and thalamus. *Biol Psychiatry* 62:429–437.
- Greicius MD, Kiviniemi V, Tervonen O, Vainionpaa V, Alahuhta S, Reiss AL, Menon V. 2008. Persistent default-mode network connectivity during light sedation. *Hum Brain Mapp* 29:839–847.
- Greicius MD, Krasnow B, Reiss AL, Menon V. 2003. Functional connectivity in the resting brain: a network analysis of the default mode hypothesis. *Proc Natl Acad Sci U S A* 100:253–258.
- Greicius MD, Srivastava G, Reiss AL, Menon V. 2004. Default-mode network activity distinguishes Alzheimer’s disease from healthy aging: evidence from functional MRI. *Proc Natl Acad Sci U S A* 101:4637–4642.
- Hamilton JP, Furman DJ, Chang C, Thomason ME, Dennis E, Gotlib IH. 2011. Default-mode and task positive network activity in major depressive disorder: implications for adaptive and maladaptive rumination. *Biol Psychiatry* 70:327–333.
- Hampson M, Peterson BS, Skudlarski P, Gatenby JC, Gore JC. 2002. Detection of functional connectivity using temporal correlations in MR images. *Hum Brain Mapp* 150:247–262.
- Horowitz B. 2003. The elusive concept of brain connectivity. *NeuroImage* 190:466–470.
- Horowitz SG, Fukunaga M, de Zwart JA, van Gelderen P, Fulton SC, Balkin TJ, Duyn JH. 2008. Low frequency BOLD fluctuations during resting wakefulness and light sleep: a simultaneous EEG-fMRI study. *Hum Brain Mapp* 29:671–682.
- Kelly AM, Uddin LQ, Biswal BB, Castellanos FX, Milham MP. 2008. Competition between functional brain networks mediates behavioral variability. *Neuroimage* 39:527–537.
- Kim JH, Lee JM, Jo HJ, Kim SH, Lee JH, Kim ST, Seo SW, Cox RW, Na DL, Kim SI, Saad ZS. 2010. Defining functional SMA and pre-SMA subregions in human MFC using resting state fMRI: functional connectivity-based parcellation method. *Neuroimage* 49:2375–2386.
- Koshino H, Carpenter PA, Minshew NJ, Cherkassky VL, Keller TA, Just MA. 2005. Functional connectivity in an fMRI working memory task in high-functioning autism. *NeuroImage* 240:810–821.
- Lancaster JL, et al. 2000. Automated Talairach atlas labels for functional brain mapping. *Hum Brain Mapp* 10:120–131.
- Latora V, Marchiori M. 2001. Efficient behavior of small-world networks. *Phys Rev Lett* 87:198701–198704.
- Maldjian JA, Laurienti PJ, Kraft RA, Burdette JH. 2003. An automated method for neuroanatomic and cytoarchitectonic atlas-based interrogation of fMRI data sets. *NeuroImage* 19:1233–1239.
- Margulies DS, Kelly AM, Uddin LQ, Biswal BB, Castellanos FX, Milham MP. 2007. Mapping the functional connectivity of anterior cingulate cortex. *NeuroImage* 37:579–588.
- Mennes M, Kelly C, Zuo XN, Di Martino A, Biswal BB, Castellanos FX, Milham MP. 2010. Inter-individual differences in resting-state functional connectivity predict task-induced BOLD activity. *Neuroimage* 50:1690–1701.
- Murphy K, Birn RM, Handwerker DA, Jones TB, Bandettini PA. 2009. The impact of global signal regression on resting state correlations: are anti-correlated networks introduced? *Neuroimage* 44:893–905.
- Power JD, Barnes KA, Snyder AZ, Schlaggar BL, Petersen SE. 2012. Spurious but systematic correlations in functional

- connectivity MRI networks arise from subject motion. *Neuroimage* 59:2142–2154.
- Raichle ME, MacLeod AM, Snyder AZ, Powers WJ, Gusnard DA, Shulman GL. 2001. A default mode of brain function. *Proc Natl Acad Sci U S A* 98:676–682.
- Rissman J, Gazzaley A, D'Esposito M. 2004. Measuring functional connectivity during distinct stages of a cognitive task. *NeuroImage* 230:752–763.
- Roy AK, Shehzad Z, Margulies DS, Kelly AM, Uddin LQ, Gotimer K, Biswal BB, Castellanos FX, Milham MP. 2009. Functional connectivity of the human amygdala using resting state fMRI. *Neuroimage* 45:614–626.
- Salvador R, Suckling J, Schwarzbauer C, Bullmore E. 2005. Undirected graphs of frequency-dependent functional connectivity in whole brain networks. *Philos Trans R Soc Lond B Biol Sci* 360:937–946.
- Satterthwaite TD, Wolf DH, Loughhead J, Ruparel K, Elliott MA, Hakonarson H, Gur RC, Gur RE. 2012. Impact of in-scanner head motion on multiple measures of functional connectivity: Relevance for studies of neurodevelopment in youth. *Neuroimage* 60:623–632.
- Siegle GJ, Thompson W, Carter CS, Steinhauer SF, Thase, ME. 2007. Increased amygdala and decreased dorsolateral prefrontal BOLD responses in unipolar depression: related and independent features. *Biol Psychiatry* 610:198–209.
- Shehzad Z, Kelly AM, Reiss PT, Gee DG, Gotimer K, Uddin LQ, Lee SH, Margulies DS, Roy AK, Biswal BB, Petkova E, Castellanos FX, Milham MP. 2009. The resting brain: unconstrained yet reliable. *Cereb Cortex* 19:2209–2229.
- Stevens M, Pearlson GD, Calhoun VD. 2009. Changes in the interaction of resting state neural networks from adolescence to adulthood. *Hum Brain Mapp* 30:2356–2366.
- Uddin LQ, Kelly AM, Biswal BB, Castellanos FX, Milham MP. 2009. Functional connectivity of default mode network components: correlation, anticorrelation, and causality. *Hum Brain Mapp* 30:625–637.
- Uddin LZ, Supekar K, Amin H, Rykhlevskaia E, Nguyen DA, Greicius MD, Menon V. 2010. Dissociable connectivity within human angular gyrus and intraparietal sulcus: evidence from functional and structural connectivity. *Cereb Cortex* 20:2636–2646.
- Van Dijk KR, Hedden T, Venkataraman A, Evans KC, Lazar SW, Buckner RL. 2010. Intrinsic functional connectivity as a tool for human connectomics: theory, properties, and optimization. *J Neurophysiol* 103:297–321.
- Van Dijk KR, Sabuncu MR, Buckner RL. 2012. The influence of head motion on intrinsic functional connectivity MRI. *Neuroimage* 59:431–438.
- Vincent JL, Patel GH, Fox MD, Snyder AZ, Baker JT, Van Essen DC, Zempel JM, Snyder LH, Corbetta M, Raichle ME. 2007. Intrinsic functional architecture in the anaesthetized monkey brain. *Nature* 447:83–86.
- Wang K, Liang M, Wang L, Tian L, Zhang X, Li K, Jiang T. 2007. Altered functional connectivity in early Alzheimer's disease: a resting-state fMRI study. *Hum Brain Mapp* 28:967–978.
- Watts DJ, Strogatz SH. 1998. Collective dynamics of “small-world” networks. *Nature* 393:440–442.
- Weissenbacher A, Kasess C, Gerstl F, Lanzenberger R, Moser E, Windischberger C. 2009. Correlations and anticorrelations in resting-state functional connectivity MRI: a quantitative comparison of preprocessing strategies. *Neuroimage* 47:1408–1416.
- Weng SJ, Wiggins JL, Peltier SJ, Carrasco M, Risi S, Lord C, Monk CS. 2010. Alterations of resting state functional connectivity in the default network in adolescents with autism spectrum disorder. *Brain Res* 1313:202–214.
- Whitfield-Gabrieli S, Ford J. 2012. Assessment of default mode network activity and connectivity in psychopathology. *Annu Rev Clin Psychol* 8:49–76.
- Whitfield-Gabrieli S, Thermenos HW, Milanovic S, Tsuang MT, Faraone SV, McCarley RW, Shenton ME, Green, AI, Nieto-Castanon A, LaViolette P, Wojcik J, Gabrieli J, Seidman LJ. 2009. Hyperactivity and hyperconnectivity of the default network in schizophrenia and in first-degree relatives of persons with schizophrenia. *Proc Natl Acad Sci U S A* 106:1279–1284.
- Zuo XN, Di Martino A, Kelly C, Shehzad ZE, Gee DG, Klein DF, Castellanos FX, Biswal BB, Milham MP. 2010a. The oscillating brain: complex and reliable. *Neuroimage* 49:1432–1445.
- Zuo XN, Kelly C, Adelstein JS, Klein DF, Castellanos FX, Milham MP. 2010b. Reliable intrinsic connectivity networks: Test-retest evaluation using ICA and dual regression approach. *Neuroimage* 49:2163–2177.

Address correspondence to:

Susan Whitfield-Gabrieli

*Department of Brain and Cognitive Sciences
Martinos Imaging Center at McGovern Institute
for Brain Research
Poitras Center for Affective Disorders Research
Massachusetts Institute of Technology
Cambridge, MA 02139*

E-mail: swg@mit.edu

Appendix

Appendix A.1: Treatment of Temporal Confounding Factors

The observed raw blood oxygen level-dependent (BOLD) contrast signal $s(x, t)$ at voxel x and time t is characterized as a linear combination of (1) N temporal confounds defined explicitly through subject- and session-specific time series $c_n(t)$ (e.g., representing subject motion effects); (2) those confounds defined implicitly from K noise region of interests (ROIs), each characterized by M_k principal component time series

$d_{kn}(t)$ (e.g., representing physiological effects observable in white matter and CSF areas); and (3) an underlying BOLD time series of interest $e(x, t)$:

$$s(x, t) = \sum_{n=1}^N \hat{a}_n(x) \cdot c_n(t) + \sum_{k=1}^K \sum_{n=1}^{M_k} \hat{b}_{kn}(x) \cdot d_{kn}(t) + e(x, t) \quad (\text{A.1.1})$$

where $a_n(x)$ and $b_{kn}(x)$ represent voxel-specific weights for each of the confounding factors. The factors $a_n(x)$ and $b_n(x)$

are estimated using ordinary least squares, and the BOLD signal of interest $e(x,t)$ is approximated as the residuals in the linear model fit. The noise ROI time series $d_{kn}(t)$ for each ROI k are estimated using principal component analysis of the time series $s(x,t)$ limited to within ROI voxels [and after an initial orthogonalization with respect to the known $c_n(t)$ factors].

$$e^*(x,t) = s(x,t) - \sum_{n=1}^N \hat{a}_n(x) \cdot c_n(t)$$

$$d_{k1}(t) = \frac{1}{|\Omega_k|} \sum_{x \in \Omega_k} e^*(x,t)$$

$$d_{kn}(t)_{(n=2 \dots M_k)} \Big| \frac{1}{|\Omega_k|} \sum_{x \in \Omega_k} (e^*(x,u) - d_{k1}(u)) \cdot (e^*(x,\nu) - d_{k1}(\nu))$$

$$= \sum_{n=2}^T d_{kn}(u) \cdot d_{kn}(\nu)$$

$$\sum_{t=1}^T d_{kn}(t) \cdot d_{km}(t) = 0 \quad \forall 1 < n < m$$

$$\sum_{t=1}^T d_{kn}^2(t) \geq \sum_{t=1}^T d_{km}^2(t) \quad \forall 1 < n < m$$

Where $d_{k1}(t)$ represents the average residual BOLD time series within the ROI voxels W_{k1} and $d_{kn}(t)$ (for $1 < n \leq M_k$) represents the first M_k-1 principal components of the temporal covariance matrix within the same voxels. The initial orthogonalization in $e^*(x,t)$ guarantees that the noise ROI time series $d_{kn}(t)$ are in turn orthogonal to the confounding factor time series $c_n(t)$, making the resulting model (1) maximally predictive.

This approach assumes that the BOLD signal of interest $e(x,t)$ is orthogonal to each confounding factors $c_n(t)$ and $d_{kn}(t)$. While this can lead to decreased sensitivity in those cases where the signal of interest is in fact correlated with some of the confounding factors, we believe that the increased robustness and validity of the resulting functional connectivity measures compensates the decreased sensitivity in these cases.

Appendix A.2: Computing Voxel-Wise Linear Functional Connectivity Measures Singular Value Decomposition

We represent the raw BOLD signal at voxel x and time t as $s(x,t)$. We are interested in computing the functional connectivity matrix \mathbf{R} , characterizing the temporal correlation between the BOLD signal at two arbitrary voxels x_1 and x_2 :

$$\mathbf{R}: r(x_1, x_2) \equiv \sum_t \tilde{s}(x_1, t) \cdot \tilde{s}(x_2, t) \quad (\text{A.2.1})$$

where $\tilde{s}(x,t)$ represents the normalized BOLD time series (after subtracting its mean, and dividing by its standard deviation). Typically the number of voxels is considerably larger than the number of time points (scans). Because of this it is more efficient to compute the crosscovariance matrix (time-by-time covariance matrix, aggregated across all brain voxels W), and to perform a singular value decomposition as follows:

$$\mathbf{C}: c(t_1, t_2) \equiv \sum_{x \in \Omega} \tilde{s}(x, t_1) \cdot \tilde{s}(x, t_2) = \sum_n d_n \cdot q_n(t_1) \cdot q_n(t_2)$$

From this decomposition we can define a new set of maps \mathbf{b}_n as:

$$\mathbf{b}_n: b_n(x) \equiv \sum_t q_n(t) \cdot \tilde{s}(x, t)$$

This decomposition allows a simple reconstruction of the voxel-to-voxel BOLD signal temporal correlation matrix \mathbf{R} as:

$$\mathbf{R}: r(x_1, x_2) = \sum_n b_n(x_1) \cdot b_n(x_2) \quad (\text{A.2.2})$$

In this way the \mathbf{b}_n maps (eigenvectors) and associated d_n values (eigenvalues) implicitly characterize the correlation matrix \mathbf{R} . In the presence of band-pass filtering the number of independent eigenvectors n is significantly smaller than the number of independent time points (scans), so storing the $b_n(x)$ maps requires always less storage than a copy of the original functional data $s(x,t)$. In addition, many measures derived from the matrix \mathbf{R} can easily be computed without ever requiring to explicitly estimate the elements of this matrix as the following section will illustrate.

Derived Measures

It can be shown that the \mathbf{b}_n maps form an orthogonal basis[†] for the entire set of possible connectivity maps (the row or column space of \mathbf{R}). For example, an entire voxel-to-voxel connectivity map with voxel x_1 as seed (one row of \mathbf{R}) can be computed as follows:

$$\mathbf{r}(x_1) = \sum_n b_n(x_1) \cdot \mathbf{b}_n$$

And the average of several connectivity maps (averaging several rows of \mathbf{R} , e.g., those corresponding to voxels within a given seed ROI X) can be computed as follows:

$$\mathbf{r}(X) \equiv \langle \mathbf{r}(x) \rangle_{x \in X} = \sum_n \bar{b}_n(X) \cdot \mathbf{b}_n$$

where $\bar{b}_n(X)$ represents the average value of the \mathbf{b}_n map at the voxels within the ROI X .

The norm of these connectivity maps, a measure of the overall strength of each connectivity map averaged across all target voxels (corresponding to the norm of one row of \mathbf{R}), can be computed, respectively, and with minimal computation as follows:

$$\|\mathbf{r}(x_1)\|^2 \equiv \sum_{x_2 \in \Omega} r^2(x_1, x_2) = \sum_n d_n \cdot b_n^2(x_1)$$

$$\|\mathbf{r}(X)\|^2 \equiv \sum_{x_2 \in \Omega} \langle r(x_1, x_2) \rangle_{x_1 \in X}^2 = \sum_n d_n \cdot \bar{b}_n^2(X)$$

The average voxel-to-voxel connectivity between two ROIs x_1 and x_2 (averaging the values within a submatrix of \mathbf{R}) can also be computed with minimal computation[‡] as follows:

[†]Not orthonormal, as the squared-norm of each \mathbf{b}_n map equals d_n .

[‡]For example, we can consider the costs associated with computing the average connectivity between any two arbitrary pairs of ROIs in one atlas encompassing the entire set of brain voxels. Using (1) we would need to compute all voxel-to-voxel connectivity values first and then average across the desired ROIs. This computation scales quadratically with the number of voxels, which is usually prohibitive both in terms of time and required memory storage. Using (2) instead, this computation scales linearly with the number of voxels, as it only requires computing the average values of the \mathbf{b} maps within each ROI (no voxel-wise cross-products involved).

$$\bar{r}(X_1, X_2) \equiv \langle r(x_1, x_2) \rangle_{x_1 \in X_1, x_2 \in X_2} = \sum_n \bar{b}_n(X_1) \cdot \bar{b}_n(X_2)$$

In addition, several complex measures derived from voxel-wise connectivity measures can also be computed with reduced computational cost. For example, the map of differential connectivity between two voxels x_1 and x_2 can be computed as follows:

$$\mathbf{r}(x_1) - \mathbf{r}(x_2) = \sum_n (b_n(x_1) - b_n(x_2)) \cdot \mathbf{b}_n$$

The overall strength of this differential connectivity map, a measure of the difference between the two individual connectivity maps (similar to η^2 measure in Cohen et al., 2008), can be computed as follows:

$$\begin{aligned} \|\mathbf{r}(x_1) - \mathbf{r}(x_2)\|^2 &\equiv \sum_{x \in \Omega} (r(x_1, x) - r(x_2, x))^2 \\ &= \sum_n d_n \cdot (b_n(x_1) - b_n(x_2))^2 \end{aligned}$$

Similarly, the functional similarity measure between voxels x_1 and x_2 (Kim et al., 2010), another way to characterize the difference between two individual connectivity maps, can be computed as follows:

$$S^{-1}(x_1, x_2) \equiv \sum_{x \in \Omega} r(x_1, x) \cdot r(x_2, x) = \sum_n d_n \cdot b_n(x_1) \cdot b_n(x_2)$$

The integrated local correlation measure (Deshpande et al., 2007), characterizing the average connectivity between a voxel and its neighbors (where the neighborhood is defined by a spatial convolution kernel h), can be computed as follows:

$$ILC(x_1) \equiv \langle r(x_1, x_2) \rangle_{x_2 \in \Delta(x_1)} = \sum_n b_n(x_1) \cdot (h * b_n)(x_1)$$

Similarly, the radial correlation contrast vector measure (Goelman, 2004) can also be computed using multiple convolution kernels (one for each spatial dimension), jointly defining the difference vector for each neighboring voxel.

$$\begin{aligned} RCC(x_1) &= \sum_n b_n(x_1) \cdot [(h_i * b_n)(x_1) \cdot \vec{i} + (h_j * b_n)(x_1) \cdot \vec{j} \\ &\quad + (h_k * b_n)(x_1) \cdot \vec{k}] \end{aligned}$$

Last, the norm of the local spatial gradient of a connectivity map (a measure of the similarity between the global connectivity patterns of neighboring voxels) can be computed as follows:

$$\begin{aligned} \|(\nabla \mathbf{r})(x_1)\|^2 &= \sum_n d_n \cdot \|(\nabla \mathbf{b}_n)(x_1)\|^2 \\ &= \sum_n d_n \cdot ((\partial_i \mathbf{b}_n)^2(x_1) + (\partial_j \mathbf{b}_n)^2(x_1) + (\partial_k \mathbf{b}_n)^2(x_1)) \end{aligned}$$

Comparing Connectivity Patterns Across Conditions

In an experimental design with multiple conditions (e.g., block design) we might wish to compute the task- or condition-specific connectivity matrices.

$$\mathbf{R}^A: r^A(x_1, x_2) \equiv \sum_{t \in A} \tilde{s}(x_1, t) \cdot \tilde{s}(x_2, t)$$

$$\mathbf{R}^B: r^B(x_1, x_2) \equiv \sum_{t \in B} \tilde{s}(x_1, t) \cdot \tilde{s}(x_2, t)$$

where A and B represent the time points associated with two conditions of interest. For any given seed voxel x_1 , the between-conditions correlation, a measure of the similarity between the connectivity patterns during two different conditions, separately for each seed voxel and for each subject, can be computed as follows:

$$\begin{aligned} \text{corr}(\mathbf{r}^A(x_1), \mathbf{r}^B(x_1)) &= \frac{\sum_{m,n} (d_{m,n}^{A,B} - N \cdot \bar{b}_m^A \cdot \bar{b}_n^B) \cdot b_m^A(x_1) \cdot b_n^B(x_1)}{\left(\sum_n (d_n^A - N \cdot \bar{b}_n^A) \cdot b_n^A(x_1) \cdot \sum_n (d_n^B - N \cdot \bar{b}_n^B) \cdot b_n^B(x_1) \right)^{1/2}} \end{aligned}$$

where N is the total number of voxels, \bar{b}_n^A represents the average (across all voxels) of the b_n^A component map, and the matrix $\mathbf{D}^{A,B}$ represents the between-conditions covariance matrix:

$$\mathbf{D}^{A,B}: d_{m,n}^{A,B} \equiv \sum_{x \in \Omega} b_m^A(x) \cdot b_n^B(x) \quad (\text{note: } d_{m,n}^{A,A} = d_n^A \cdot \delta_{m-n})$$

One possible application of this between-conditions correlation measure is exemplified in this article in the voxel-to-voxel analysis subsection of the results.

This article has been cited by:

1. Moriah E. Thomason, Maria A. Tocco, Kelly A. Quednau, Andrea R. Bedway, Justin M. Carré. 2013. Idle Behaviors of the Hippocampus Reflect Endogenous Cortisol Levels in Youth. *Journal of the American Academy of Child & Adolescent Psychiatry* 52:6, 642-652.e1. [[CrossRef](#)]
2. Sheeba Arnold Anteraper, Susan Whitfield-Gabrieli, Boris Keil, Steven Shannon, John D. Gabrieli, Christina Triantafyllou. Exploring Functional Connectivity Networks with Multichannel Brain Array Coils. *Brain Connectivity*, ahead of print. [[Abstract](#)] [[Full Text HTML](#)] [[Full Text PDF](#)] [[Full Text PDF with Links](#)]
3. S.M. Hadi Hosseini, Shelli R. Kesler. 2013. Comparing connectivity pattern and small-world organization between structural correlation and resting-state networks in healthy adults. *NeuroImage* . [[CrossRef](#)]
4. Virve Vuontela, Ping Jiang, Maksym Tokariev, Petri Savolainen, YuanYe Ma, Eeva T. Aronen, Tuija Fontell, Tiina Liiri, Matti Ahlström, Oili Salonen, Synnöve Carlson. 2013. Regulation of brain activity in the fusiform face and parahippocampal place areas in 7–11-year-old children. *Brain and Cognition* 81:2, 203-214. [[CrossRef](#)]
5. Salvatore Torrisi, Teena D Moody, Nathalie Vizueta, Moriah E Thomason, Martin M Monti, Jennifer D Townsend, Susan Y Bookheimer, Lori L Altshuler. 2013. Differences in resting corticolimbic functional connectivity in bipolar I euthymia. *Bipolar Disorders* 15:2, 156-166. [[CrossRef](#)]
6. William D.S. Killgore, Zachary J. Schwab, Maia Kipman, Sophie R. DelDonno, Mareen Weber. 2013. Insomnia-related complaints correlate with functional connectivity between sensory–motor regions. *NeuroReport* 24:5, 233-240. [[CrossRef](#)]